

# Orderly layer-by-layered TiO<sub>2</sub>/carbon superstructures based on MXene's defect engineering for efficient hydrogen evolution

Xianglong Kong<sup>a</sup>, Peng Gao<sup>a,b,\*</sup>, Rui Jiang<sup>a</sup>, Jing Feng<sup>a</sup>, Piaoping Yang<sup>a,\*\*</sup>, Shili Gai<sup>a</sup>, Yujin Chen<sup>c,\*\*</sup>, Qianqian Chi<sup>b</sup>, Fuchun Xu<sup>b</sup>, Wei Ye<sup>b,\*\*</sup>

<sup>a</sup> College of Materials Science and Chemical Engineering, Harbin Engineering University, Harbin, Heilongjiang, 150001, PR China

<sup>b</sup> College of Material, Chemistry and Chemical Engineering, Hangzhou Normal University, Hangzhou, Zhejiang, 311121, PR China

<sup>c</sup> College of Science, Harbin Engineering University, Harbin, Heilongjiang, 150001, PR China

## ARTICLE INFO

### Keywords:

Defect engineering

Layer-by-layer

Superstructure

MXene

TiO<sub>2</sub>/carbon

Photocatalysis

## ABSTRACT

In the development of two-dimension (2D) materials, constructing orderly layer-by-layered heterostructure has been a formidable challenge for a long time. In this work, a convenient nitriding-pretreatment route has been applied to engineer the C vacancy defects in Ti<sub>3</sub>C<sub>2</sub>T<sub>x</sub> MXene, which often results in the structural instability. Based on the above defect engineering, the 2D skeleton is maintained in the following Ti<sub>3</sub>C<sub>2</sub>T<sub>x</sub> oxidation for the formation of TiO<sub>2</sub> and carbon layers. Successfully, a “from 2D to 2D” structure and functional transformation is realized and TiO<sub>2</sub> nanoplates are in-situ grown between carbon layers, which greatly boost photogenerated carrier's separation and electron's transmission. As a result, this TiO<sub>2</sub>/C superstructure exhibits an efficient photocatalytic ability in water-splitting process under visible light without any cocatalyst (87.2 μmol g<sup>-1</sup> h<sup>-1</sup>, 28.1 times of disordered TiO<sub>2</sub>/C sample). The defect engineering for MXene provides a new strategy for the highly orderly layer-by-layer superstructure.

## 1. Introduction

Recently, two-dimension (2D) structured materials (also called van der Waals heterostructures), such as graphene [1,2], graphyne [3,4], borophene [5,6], germanene [7,8], black phosphorus [9,10] and MXene [11,12], have attracted largely attention due to their widely known thermal and electrical conductivity. These novel materials also exhibit extensively potential applications, such as photovoltaics, semiconductors, electrodes and water purification. However, to date the efficient integration of 2D functional layers with three-dimensional (3D) systems remains a significant challenge, limiting device performance and circuit design [13]. This needs a convenient and effective post-treat method to solve the above problem. Layer-by-layer self-assembling method is obviously suitable for the anticipated functionalization and complexity. In order to bypass the complex and susceptible process in currently widely used bottom-up method, a “from 2D to 2D” strategy emerges in front of us clearly. In this work, as an attempt, Ti<sub>3</sub>C<sub>2</sub>T<sub>x</sub> MXene is selected as the initial 2D skeleton to construct a new layer-by-layer TiO<sub>2</sub>/C superstructure, which undoubtedly possesses excellent carrier's separation ability to greatly enhance photocatalytic performance of semiconductor TiO<sub>2</sub>.

As a representative of photocatalysts, TiO<sub>2</sub> has been widely recognized as one of the most promising materials due to its rich reserves in nature, friendly environmental, and economical price [14–17]. However, individual TiO<sub>2</sub> still has two main disadvantages that are difficult to overcome, including wide band gap (3.2 eV for anatase) and high photogenerated carrier recombination rate [18–20]. According to previous reports, approximately 90 % of the photoelectrons and holes recombine within ~10 ns [21,22], resulting in a low photocatalytic efficiency. In the past decades, many valuable efforts have been contributed to overcome the above problems, such as scale-downing the particle size to nanometer, doping with metal or non-metal and constructing heterostructure [23–32]. Among those, carbon modified TiO<sub>2</sub> composites exhibit outstanding solar-driven H<sub>2</sub> evolution activities due to the relatively robust separation and transfer of photo-excited carriers depended on the superior conductivities of carbon materials [33–40]. More important, in evaluating photocatalytic efficiency of TiO<sub>2</sub>-based materials, light carbon doesn't have excessive additional mass effects. However, though simple core/shell TiO<sub>2</sub>/C structures have been obtained in the above works, a sufficient electron/hole separation assisted by carbon layer is still on the way. Compared with them, layer-by-layered superstructure for TiO<sub>2</sub>/C system undoubtedly will further

\* Corresponding author at: College of Material, Chemistry and Chemical Engineering, Hangzhou Normal University, Hangzhou, Zhejiang 310026, PR China.

\*\* Corresponding authors.

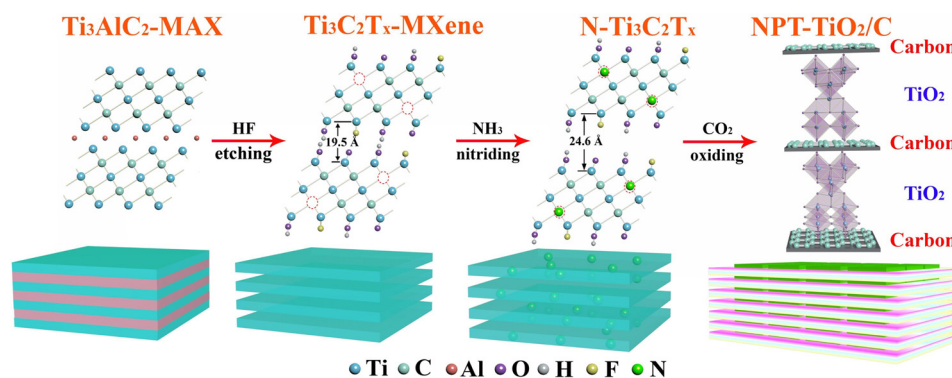
E-mail addresses: [gaopeng@hrbeu.edu.cn](mailto:gaopeng@hrbeu.edu.cn) (P. Gao), [yangpiaoping@hrbeu.edu.cn](mailto:yangpiaoping@hrbeu.edu.cn) (P. Yang), [chenyujin@hrbeu.edu.cn](mailto:chenyujin@hrbeu.edu.cn) (Y. Chen), [yewei@hznu.edu.cn](mailto:yewei@hznu.edu.cn) (W. Ye).

<https://doi.org/10.1016/j.apcata.2019.117341>

Received 28 August 2019; Received in revised form 4 November 2019; Accepted 10 November 2019

Available online 23 November 2019

0926-860X/ © 2019 Elsevier B.V. All rights reserved.



**Scheme 1.** Preparation process from  $\text{Ti}_3\text{C}_2\text{T}_x$ -MAX to  $\text{Ti}_3\text{C}_2\text{T}_x$ -MXene, N- $\text{Ti}_3\text{C}_2\text{T}_x$  and layer-by-layered NPT- $\text{TiO}_2/\text{C}$  samples.

improve the carrier's separation and promote the corresponding catalytic ability.

Directed by the above analysis, we have successfully designed and realized a convenient in situ route to synthesize highly ordered layer-by-layered superstructure composed of  $\text{TiO}_2$  and carbon layer. This process involves two critical steps: I) Defect engineering of  $\text{Ti}_3\text{C}_2\text{T}_x$ -MXene for N- $\text{Ti}_3\text{C}_2\text{T}_x$  through a nitriding-pretreatment, which strengthens the 2D skeleton and facilitates the following “from 2D to 2D” structural transformation; II)  $\text{CO}_2$  oxidation of N- $\text{Ti}_3\text{C}_2\text{T}_x$ , which results in the in situ growth of  $\text{TiO}_2$  between MXene's layers and the eventual  $\text{TiO}_2/\text{C}$  layer-by-layered superstructure (NPT- $\text{TiO}_2/\text{C}$ ), as shown in Scheme 1. The intercalation superstructure could efficiently strengthen the photoexcited carrier's separation and transfer more electrons into suitable photocatalytic sites, thus facilitating the hydrogen reduction through water splitting. The as-obtained NPT- $\text{TiO}_2/\text{C}$  superstructure exhibits a highest  $\text{H}_2$  evolution rate up to 87.2 and  $425.6 \mu\text{mol g}^{-1} \text{h}^{-1}$  respectively under visible-light and simulated sunlight without any co-catalyst, which are about 28.1 times and 8.2 times of those of simple  $\text{TiO}_2/\text{C}$  composite.

## 2. Experimental section

### 2.1. Synthesis of $\text{Ti}_3\text{C}_2\text{T}_x$ -MXene

1g of  $\text{Ti}_3\text{AlC}_2$  powder was divided into multiple portions and then slowly added to HF solution with a 49 % concentration. Then the above suspension was placed in a magnetic stirrer to maintain at  $40^\circ\text{C}$  for 36 h. After that the mixture was washed with deionized water by multiple high-speed centrifugation (5000 rpm) until the pH of the supernatant was up to approximately 7. Finally, the sample was kept in a vacuum oven ( $60^\circ\text{C}$ ) for 12 h.

### 2.2. Synthesis of N- $\text{Ti}_3\text{C}_2\text{T}_x$

The above as-prepared  $\text{Ti}_3\text{C}_2\text{T}_x$  MXene powder was transferred into a tube furnace and kept in argon gas stream for 1 h. After that, the tube furnace was continuously fed with ammonia gas ( $100 \text{ mL min}^{-1}$ ) for 2 h at  $300^\circ\text{C}$ .

### 2.3. Synthesis of disordered $\text{TiO}_2/\text{C}$ and NPT- $\text{TiO}_2/\text{C}$ superstructure

The as-synthesized N- $\text{Ti}_3\text{C}_2\text{T}_x$  MXene powder was putted into a tube furnace under carbon dioxide atmosphere ( $100 \text{ mL min}^{-1}$ ) for 2 h at  $700^\circ\text{C}$  and then naturally cooled to room temperature. The disordered  $\text{TiO}_2/\text{C}$  sample was fabricated in the same condition, in which only N- $\text{Ti}_3\text{C}_2\text{T}_x$  powder is replaced by  $\text{Ti}_3\text{C}_2\text{T}_x$  MXene powder.

## 3. Results and discussion

### 3.1. Defect engineering of $\text{Ti}_3\text{C}_2\text{T}_x$ MXene through a nitriding-pretreatment

It is well known that there are many residual defects, such as C vacancy defect, Ti defect and redundant functional groups (such as -F and -OH) existed in  $\text{Ti}_3\text{C}_2\text{T}_x$  MXene [41–44], which often initiate structural instability and variable property in the following chemical treatment. So in this work, a nitriding-pretreatment of  $\text{Ti}_3\text{C}_2\text{T}_x$

MXene is firstly conducted to engineer the C vacancy defect. As illustrated in Figs. 1a–c and S1a, b, the morphologies of the  $\text{Ti}_3\text{AlC}_2$ -MAX precursor, the as-obtained  $\text{Ti}_3\text{C}_2\text{T}_x$ -MXene and N- $\text{Ti}_3\text{C}_2\text{T}_x$  samples are observed by SEM examinations. It is seen that the  $\text{Ti}_3\text{C}_2\text{T}_x$ -MXene obtained by HF etching of the  $\text{Ti}_3\text{AlC}_2$ -MAX precursor presents a distinct stacked 2D layered structure. It is also noted that N- $\text{Ti}_3\text{C}_2\text{T}_x$  (Fig. 1c) obtained by an ammonia nitriding-pretreatment maintains almost a similar layered structure to  $\text{Ti}_3\text{C}_2\text{T}_x$ . Microstructural differences are observed in their XRD patterns, as shown in Figs. 1d and S2. It is seen that the (002) diffraction peak belonged to the stacked Ti-C layers, shifts from  $9.03^\circ$  to  $7.22^\circ$ , which means that the layer spacing is increased from  $19.5 \text{ \AA}$  to  $24.6 \text{ \AA}$ . Therefore, the introduction of N into MXene not only maintains the 2D-skeleton, but also increases the interlayer spacing by  $5.1 \text{ \AA}$ , which is favorable for the following intercalation of  $\text{TiO}_2$ . Fig. 1e and Table S1 show the N 1s XPS spectra and corresponding peak analyses of  $\text{Ti}_3\text{C}_2\text{T}_x$ -MXene before and after nitriding-pretreatment. The appearance of N-Ti at  $396.6 \text{ eV}$  and N-Ti-O at  $399.5 \text{ eV}$  suggests that N atoms have been successfully introduced [45–48]. And interestingly the former agrees with the N 1s XPS spectrum in the  $\text{Ti}_4\text{N}_3\text{T}_x$ -MXene [49], which means that partial N atoms are introduced into C atom sites in  $\text{Ti}_3\text{C}_2\text{T}_x$ -MXene. And the latter (N- $\ominus$  TiO-) suggests that the residual -F and -OH on surface are substituted and dramatically reduced (Fig. S3a, 4 and Table S2). The presence of carbon vacancy defects in  $\text{Ti}_3\text{C}_2\text{T}_x$ -MXene is also confirmed by EPR spectra (Fig. 1f), in which a strong signal at  $g = 2.004$  is exhibited [50,51]. After the nitriding-pretreatment of the MXene, the above signal completely disappeared, which testifies the elimination of carbon vacancies after N remediation, agreed with the above XPS results of the N- $\text{Ti}_3\text{C}_2\text{T}_x$  sample. In addition, the XPS survey, C 1s spectra and the corresponding analyses of  $\text{Ti}_3\text{C}_2\text{T}_x$  and N- $\text{Ti}_3\text{C}_2\text{T}_x$  (Fig. S3, Table S2 and S3) identify that the atom ratio of C/Ti doesn't change before and after the nitriding-pretreatment. Only the binding energy of C-Ti bond is reduced. All the above results confirm that the carbon vacancy defects in  $\text{Ti}_3\text{C}_2\text{T}_x$ -MXene are engineered through a nitrogen-remediating, without replacing the carbon atoms by N atoms. The N-remediating is further verified by the Raman spectra (Fig. S4), in which the Ti-N peaks are very similar to those of  $\text{Ti}_4\text{N}_3\text{T}_x$  MXene [52].

### 3.2. $\text{CO}_2$ oxidation of N- $\text{Ti}_3\text{C}_2\text{T}_x$

Using the above  $\text{Ti}_3\text{C}_2\text{T}_x$  and N- $\text{Ti}_3\text{C}_2\text{T}_x$  samples as Ti sources for

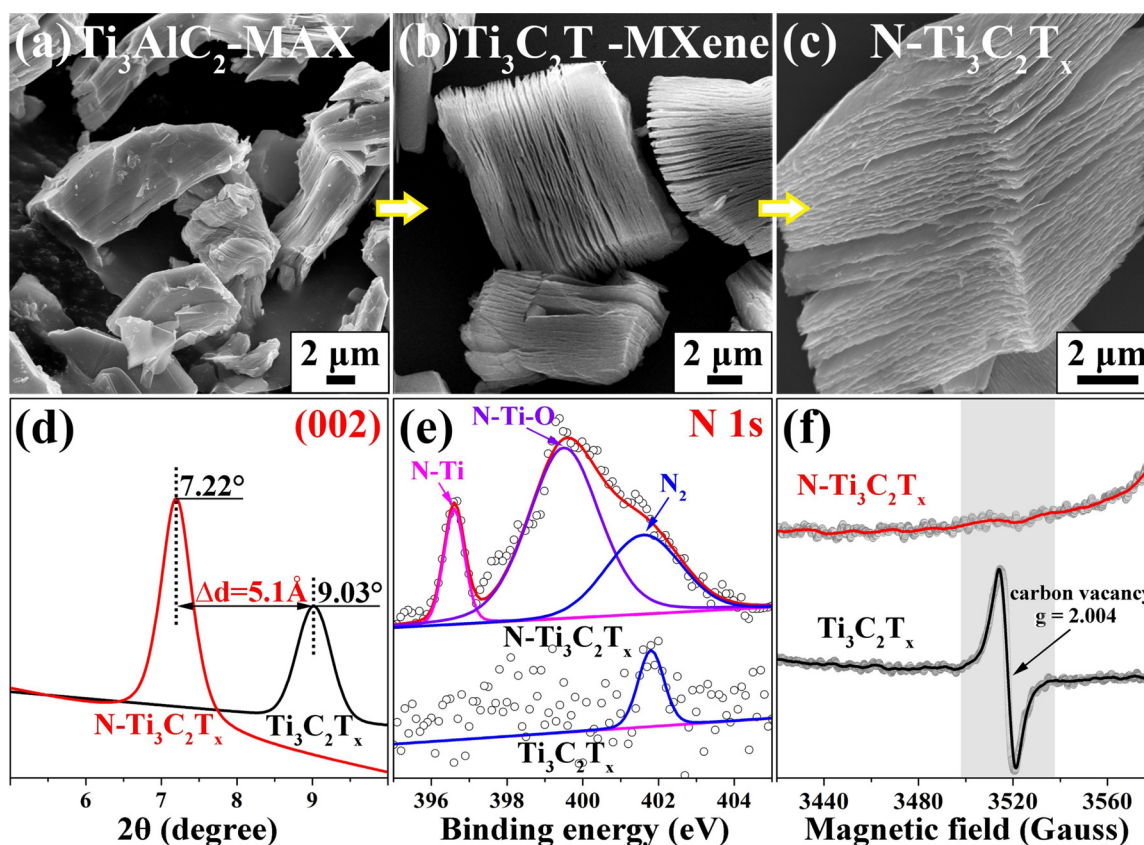


**Fig. 1.** SEM images of  $\text{Ti}_3\text{AlC}_2\text{-MAX}$  (a),  $\text{Ti}_3\text{C}_2\text{T}_x\text{-MXene}$  (b) and  $\text{N-Ti}_3\text{C}_2\text{T}_x$  (c). (d) Amplified (002) peak in XRD patterns, (e) N 1s XPS spectra and (f) EPR spectra of  $\text{Ti}_3\text{C}_2\text{T}_x\text{-MXene}$  and  $\text{N-Ti}_3\text{C}_2\text{T}_x$  samples.

$\text{TiO}_2$ , same  $\text{CO}_2$  oxidation treatments are performed on them and the as-obtained samples are named as  $\text{TiO}_2/\text{C}$  and  $\text{NPT-TiO}_2/\text{C}$ , respectively. Fig. S5 displays their XRD patterns, in which distinct diffraction peaks of anatase and rutile  $\text{TiO}_2$  are observed and no other peaks are found. It is obvious that both  $\text{Ti}_3\text{C}_2\text{T}_x$  and  $\text{N-Ti}_3\text{C}_2\text{T}_x$  are completely converted to  $\text{TiO}_2$  after oxidation. The detailed morphologies and microstructures of them are further investigated by SEM, TEM, HRTEM, SAED and EDX mapping examinations.

It is seen from the low-resolution SEM image and TEM image (Fig. 2a and b) that the  $\text{NPT-TiO}_2/\text{C}$  sample maintains a well layered structure with many nanoparticles dispersed in them. Differently, the  $\text{TiO}_2/\text{C}$  sample without nitriding-pretreatment displays that many large particles ( $\text{TiO}_2$ ) are concentrated on the edge of layers, as depicted in Fig. S6. A typical HRTEM image is shown in Fig. 2c, in which a  $\text{TiO}_2/\text{C}$  layer-by-layer superstructure is observed. An orderly 4.8 nm layer-spacing between carbon layers is detected. In order to further characterize the superstructure, a strong ultrasonic treatment with a long-time was conducted to obtain individual sheets. As exhibited in Fig. 2d, it is observed that  $\text{TiO}_2$  nanoplates with exposed (101) crystal plane lie on the bulky amorphous carbon layer. The anatase phase of  $\text{TiO}_2$  is also demonstrated by its SAED result (Fig. S7). A piece of typical  $\text{NPT-TiO}_2/\text{C}$  superstructure with a tilted angle is also examined in detail by HRTEM, as shown in Fig. 2e–h. Clearly,  $\text{TiO}_2$  nanoplates are intercalated between carbon layers. All the above results adequately prove that  $\text{TiO}_2$  nanoplates have been successfully intercalated between carbon layers and orderly layer-by-layered  $\text{TiO}_2/\text{C}$  superstructure forms, as illustrated in its structural schematic (Fig. S8). This stacking superstructure will undoubtedly greatly promote the separation of photogenerated carriers. Correspondingly, their low-angle XRD examinations (Fig. 2i) affirm that there is uniform sized pores ( $\sim 4.8$  nm) existed in the  $\text{NPT-TiO}_2/\text{C}$  sample, as seen in its HRTEM image (Fig. 2c). This result is also verified by their following BET

measurements. As shown in Fig. 2j, it is clearly seen from the pore size distributions that the  $\text{NPT-TiO}_2/\text{C}$  sample has a highly ordered porous structure (concentrated at 4.8 nm), which agrees well with its above results. However, the pore size of the disordered  $\text{TiO}_2/\text{C}$  sample is widely distributed between 5 nm and 50 nm. At the same time, the  $\text{NPT-TiO}_2/\text{C}$  sample displays a larger surface area ( $59.10 \text{ m}^2 \text{ g}^{-1}$ ) than that of  $\text{TiO}_2/\text{C}$  ( $48.83 \text{ m}^2 \text{ g}^{-1}$ ), as exhibited in Fig. S9. So the engineering of C vacancy defect through the nitriding-pretreatment of  $\text{Ti}_3\text{C}_2\text{T}_x$  MXene is critical to the “from 2D to 2D” evolution and the eventual 2D superstructure.

Afterwards, its EDS elemental mappings in Fig. 2k–n further reveal the element composition: the tiny particle contains Ti and O elements and the bulky sheet is composed of C elements. The composition is further confirmed by Raman tests (Fig. S10). The peaks ascribed to  $\text{TiO}_2$  are found in both the  $\text{TiO}_2/\text{C}$  sample and  $\text{NPT-TiO}_2/\text{C}$  sample in the  $100 - 750 \text{ cm}^{-1}$  range (Fig. S10a). The D and G peaks of carbon layers (Fig. S10b) are also observed with a different  $I_D/I_G$  value, which proves the better structural integrality in  $\text{NPT-TiO}_2/\text{C}$  superstructure. Their corresponding XPS and FT-IR results also testify the existence of  $\text{TiO}_2$  and amorphous carbon, as well as the complete disappearance of  $\text{N-Ti}_3\text{C}_2\text{T}_x$  in  $\text{NPT-TiO}_2/\text{C}$ , as shown in Figs. S11–S13 and Table S4.

### 3.3. Optical and electrical properties

The UV–vis DRS measurements were firstly applied to explore the optical absorption performance and band structures of disordered  $\text{TiO}_2/\text{C}$  and  $\text{NPT-TiO}_2/\text{C}$  superstructure with the same test amount. It is clearly seen in Fig. 3a that compared with the  $\text{TiO}_2/\text{C}$  sample, light absorption of  $\text{NPT-TiO}_2/\text{C}$  sample is significantly enhanced from UV range to the visible-light range. One of the main reasons is its orderly porous structure, which results in the multiple reflection and sufficient contact between incident light and  $\text{NPT-TiO}_2/\text{C}$  sample. Based on the

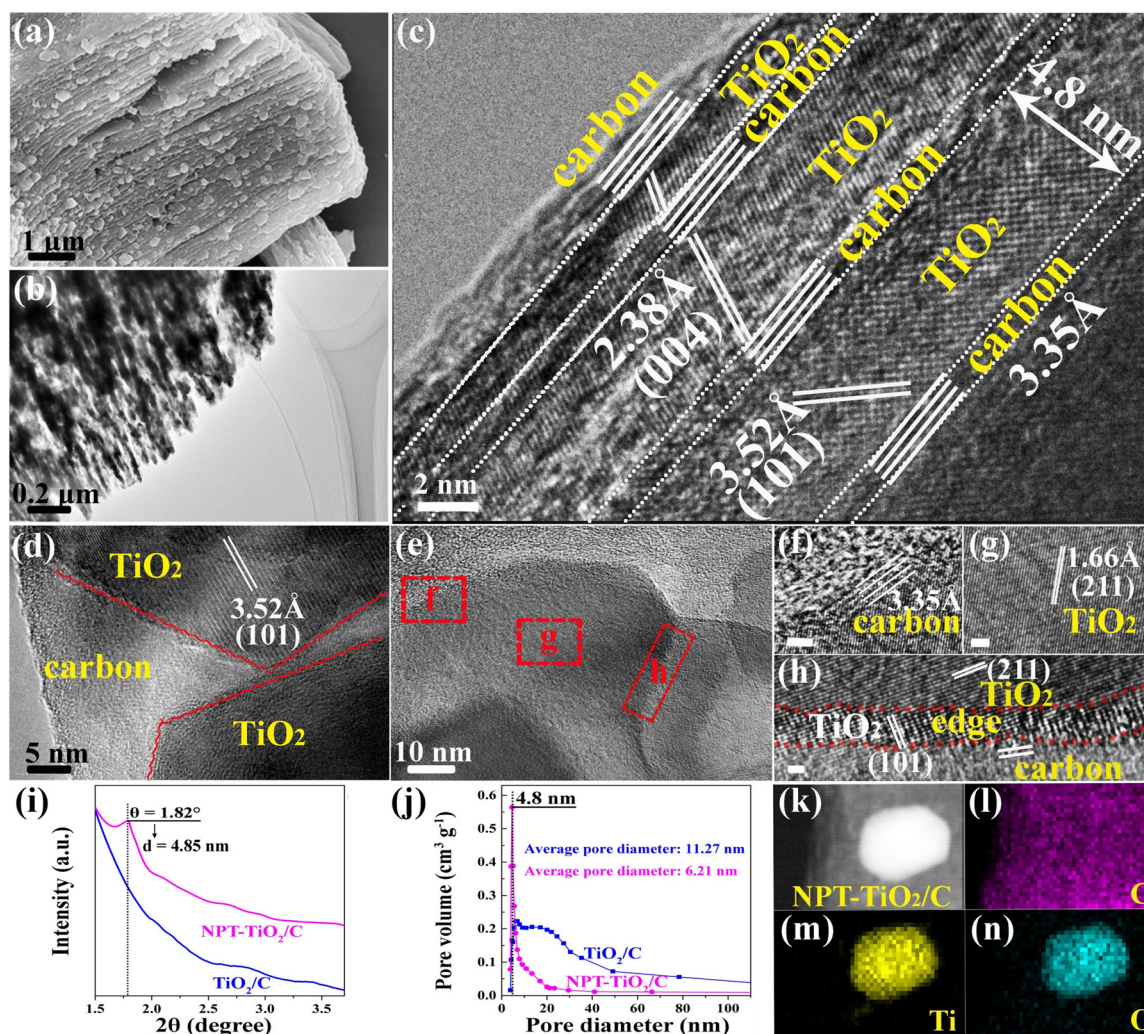


**Fig. 2.** (a) SEM image, (b)–(h) TEM and HRTEM images of NPT-TiO<sub>2</sub>/C sample. (i) Low-angle XRD patterns and (j) Pore size distribution curves of the TiO<sub>2</sub>/C and NPT-TiO<sub>2</sub>/C samples. (k)–(n) HAADF-STEM image of NPT-TiO<sub>2</sub>/C sample and its corresponding EDS mappings. Scale bars, (f)–(h) 1 nm.

transformed plot of UV–vis DRS by Kubelka-Munk formula, the band gaps of P25-TiO<sub>2</sub>, TiO<sub>2</sub>/C and NPT-TiO<sub>2</sub>/C superstructure are calculated as 3.27, 3.39 and 2.71 eV respectively (Fig. S14 and inset of Fig. 3a) with a 0.68 eV difference. The narrowed band gap of the NPT-TiO<sub>2</sub>/C sample should be owing to the superior contact between conductive carbon layer and TiO<sub>2</sub> nanoplates in the layer-by-layered superstructure. This is also confirmed by their valence band (VB) spectra. It is seen in Fig. 3b that the approximate VB tops of TiO<sub>2</sub>/C and NPT-TiO<sub>2</sub>/C are 2.55 and 2.34 eV, respectively. Therefore, the band-gap narrowing mainly derives from the 0.47 eV change of the conduction band (CB) affected by the contacted carbon layers, as exhibited in Fig. 3c. Their conductivity is analyzed through electrochemical impedance experiments under dark and light illumination conditions, as shown in Figs. S15a and 3 d. In the semicircular Nyquist plots, the NPT-TiO<sub>2</sub>/C sample's resistance is much smaller than that of disordered TiO<sub>2</sub>/C, implying its preferable conductivity [53,54]. This is beneficial to its carrier's transportation and separation. And the NPT-TiO<sub>2</sub>/C sample displays a better ability for electron transmission even in the dark (Fig. S15a). It is observed from the Mott-Schottky plots of TiO<sub>2</sub>/C and NPT-TiO<sub>2</sub>/C (Fig. S15b) that the positive slopes in the both curves identify their nature as n-type semiconductor. In addition, through the above Mott-Schottky plots, the carrier densities (Supplementary Method 4) of TiO<sub>2</sub>/C and NPT-TiO<sub>2</sub>/C superstructure are calculated as  $9.21 \times 10^{17}$  and  $39.49 \times 10^{17} \text{ cm}^{-3}$  respectively, which indicates that the NPT-TiO<sub>2</sub>/C superstructure has a remarkably improved carrier

density (about 4.3 times) compared with the disordered TiO<sub>2</sub>/C.

Then the photo current responses of two samples were performed under visible-light irradiation. As illustrated in Fig. 3e, the transient photocurrent density of NPT-TiO<sub>2</sub>/C is up to  $75 \mu\text{A cm}^{-2}$ , which is 5 times of TiO<sub>2</sub>/C ( $15 \mu\text{A cm}^{-2}$ ). The outstanding performance is mainly due to the better visible-light absorption ability and its effective transportation of photoproducted carriers, as proved above. To further identify their carrier's separation efficiency, PL examinations were applied later with the same test amount. It is seen in Fig. 3f that the fluorescence intensity of TiO<sub>2</sub>/C is much higher than that of NPT-TiO<sub>2</sub>/C sample at a 320 nm excitation wavelength, which superstrates the lower carrier's recombination ratio in the orderly superstructure. Similar phenomena are also found in other PL spectra with 300, 340 and 360 nm excitation wavelengths (Fig. S16). The better carrier's separation ability of NPT-TiO<sub>2</sub>/C superstructure was also confirmed by the fluorescence lifetime examinations (Supplementary Method 4, Figs. 3g and S17). Compared with TiO<sub>2</sub>/C ( $\tau_a = 0.67 \text{ ns}$ ), the NPT-TiO<sub>2</sub>/C superstructure has a long carrier lifetime ( $\tau_a = 1.61 \text{ ns}$ ), which indicates that the recombination rate of carrier in the superstructure is greatly slowed down. All the above results demonstrate that the orderly superstructure dramatically accelerates the electron transfer and effectively suppresses the recombination of electron-holes compared with disordered TiO<sub>2</sub>/C, which are significantly boost to its photocatalytic ability. The schematic diagram of light-excited and photocarrier's separation of NPT-TiO<sub>2</sub>/C superstructure is exhibited in Fig. 3h.

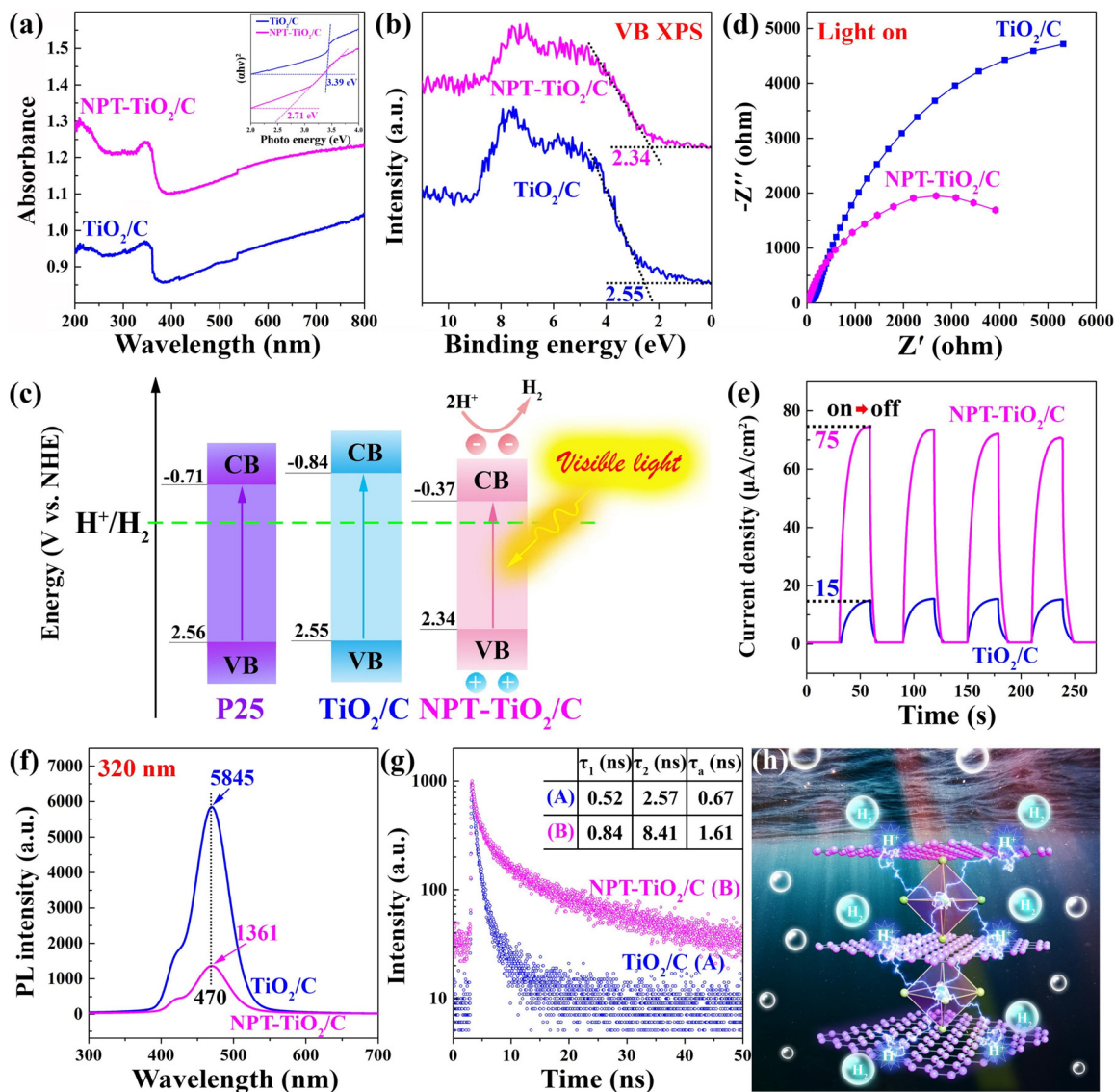


Fig. 3. Optical and electrical measurements of the TiO<sub>2</sub>/C and NPT-TiO<sub>2</sub>/C samples: (a) UV-vis DRS and their corresponding Tauc/Davis-Mott plots in the inset. (b) and (c) The VB XPS spectra and the band-gap structures. (d) and (e) EIS Nyquist plots under light irradiation and transient photocurrent density curves. (f) and (g). Photoluminescence emission curves and time-resolved transient PL decay curves. (h) Photocatalytic schematic diagram of layer-by-layered NPT-TiO<sub>2</sub>/C superstructure.

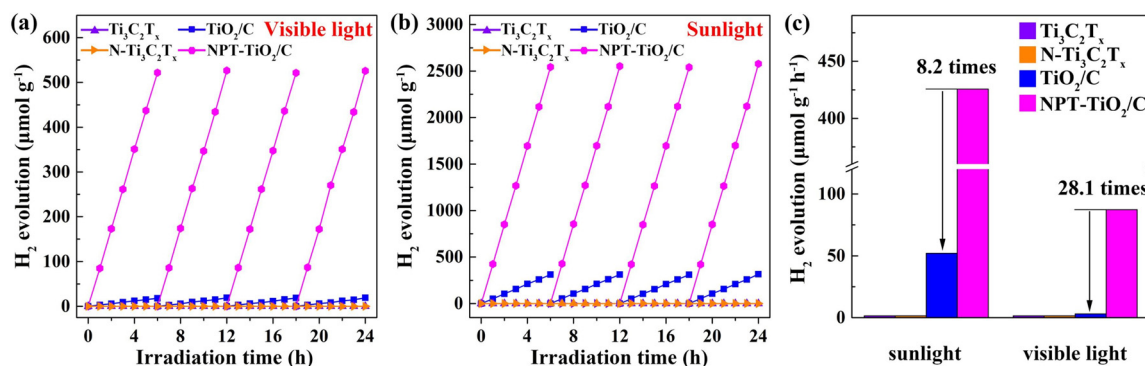


Fig. 4. Typical time course of hydrogen generation for Ti<sub>3</sub>C<sub>2</sub>T<sub>x</sub>-MXene, N-Ti<sub>3</sub>C<sub>2</sub>T<sub>x</sub>, TiO<sub>2</sub>/C and NPT-TiO<sub>2</sub>/C samples under visible light (a) and simulated sunlight (b). (c) Average hydrogen evolution rates of four samples.

### 3.4. Photocatalytic hydrogen evolution

It is seen from the results of hydrogen generation (Fig. 4a) that there is almost no hydrogen overflow during the illumination in the  $\text{Ti}_3\text{C}_2\text{T}_x$  MXene and N- $\text{Ti}_3\text{C}_2\text{T}_x$  samples. However, the  $\text{H}_2$  production rates of NPT- $\text{TiO}_2/\text{C}$  superstructure under visible light and simulated sunlight (Fig. 4a–c) without any co-catalyst are up to 87.2 and 425.6  $\mu\text{mol g}^{-1} \text{h}^{-1}$  respectively, which are about 28.1 times and 8.2 times of  $\text{TiO}_2/\text{C}$  (ca. 3.1 and 51.9  $\mu\text{mol g}^{-1} \text{h}^{-1}$  respectively). Moreover, the quantum efficiency of the superstructure is up to 1.61 % at 420 nm (Supplementary Method 4, Fig. S18a). The greatly enhanced quantum efficiency at 365, 420 and 450 nm, are exhibited in the inset (Fig. S18a) relative to that of the disordered  $\text{TiO}_2/\text{C}$  sample (only 0.11 % at 420 nm and close to zero beyond 450 nm). Meanwhile, the NPT- $\text{TiO}_2/\text{C}$  superstructure maintains a prominent generation rate of  $\text{H}_2$  (ca. 87  $\mu\text{mol g}^{-1} \text{h}^{-1}$ ) with a robust stability after recycled 240 h under visible-light illumination (Fig. S18b). It is notable that no obvious changes are found about the composition, pore structure and optical property of NPT- $\text{TiO}_2/\text{C}$  sample after hydrogen production test with 40 cycles, as exhibited in Fig. S19.

### 4. Conclusions

In conclusion, we have rationally designed and applied a nitriding-pretreatment method to remedy the C vacancy defects in  $\text{Ti}_3\text{C}_2\text{T}_x$  MXene, which guarantees the following “from 2D to 2D” structural transformation for layer-by-layered  $\text{TiO}_2/\text{C}$  superstructure. The as-obtained orderly NPT- $\text{TiO}_2/\text{C}$  superstructure displays strengthened light-absorption property and excellent photogenerated carrier's separation ability, which result in its efficient photocatalytic ability in water-splitting process under visible light without any cocatalyst (87.2  $\mu\text{mol g}^{-1} \text{h}^{-1}$ , 28.1 times of disordered  $\text{TiO}_2/\text{C}$  sample). This work opens a new window to efficiently integrate 2D structures into 3D functional superstructure.

### Declaration of Competing Interest

The authors declare no conflict of interest.

### Acknowledgements

This work was financially supported in part by the Pandeng Plan Foundation (4095C5021820406, 4095C5021820441) of Hangzhou Normal University, Zhejiang Provincial Natural Science Foundation (LY18E020010, LQ19B010001), National College Students' Science and Technology Innovation Project (No. 201910346045, 201910346038, 201910346030), National Natural Science Foundation of China (No. 51902077), Zhejiang Province “Ten Thousand People Plan”, Agricultural and Social Development Program Project (20191203B03) of Hangzhou Science and Technology Bureau of Zhejiang Province, and general items of Zhejiang Provincial Department of Education (Y201840068, Y201533640).

### Appendix A. Supplementary data

Supplementary material related to this article can be found, in the online version, at doi:<https://doi.org/10.1016/j.apcata.2019.117341>.

### References

- [1] M. Yankowitz, Q. Ma, P. Jarillo-Herrero, B.J. LeRoy, *Nat. Rev. Phys.* 1 (2019) 112–125.
- [2] L. Lin, B. Deng, J.Y. Sun, H.L. Peng, Z.F. Liu, *Chem. Rev.* 118 (2018) 9281–9343.
- [3] X. Gao, H.B. Liu, D. Wang, J. Zhang, *Chem. Soc. Rev.* 48 (2019) 908–936.
- [4] Y.J. Li, L. Xu, H.B. Liu, Y.L. Li, *Chem. Soc. Rev.* 43 (2014) 2572–2586.
- [5] X.L. Liu, Z.H. Zhang, L.Q. Wang, B.I. Yakobson, M.C. Hersam, *Nat. Mater.* 17 (2018) 783–788.
- [6] X. Liu, L. Wang, S. Li, M.S. Rahn, B.I. Yakobson, M.C. Hersam, *Nat. Commun.* 10 (2019) 1642.
- [7] L. Zhang, P. Bampoulis, A.N. Rudenko, Q. Yao, A. van Houselt, B. Poelsema, M.I. Katsnelson, H.J. Zandvliet, *Phys. Rev. Lett.* 116 (2016) 256804.
- [8] Q.H. Chen, L. Liang, G. Potsi, P.H. Wan, J.M. Lu, T. Giousis, E. Thomou, D. Gournis, P. Rudolf, J.T. Ye, *Nano Lett.* 19 (2019) 1520–1526.
- [9] J. Qiao, X. Kong, Z.X. Hu, F. Yang, W. Ji, *Nat. Commun.* 5 (2014) 4475.
- [10] H. Liu, Y. Du, Y. Deng, P.D. Ye, *Chem. Soc. Rev.* 44 (2015) 2732–2743.
- [11] M. Naguib, V.N. Mochalin, M.W. Barsoum, Y. Gogotsi, *Adv. Mater.* 26 (2014) 992–1005.
- [12] B. Anasori, M.R. Lukatskaya, Y. Gogotsi, *Nat. Rev. Mater.* 2 (2017) 16098.
- [13] Y. Xu, C. Cheng, S.C. Du, J.Y. Yang, B. Yu, J. Luo, W.Y. Yin, E. Li, S.R. Dong, P. Ye, X.F. Duan, *ACS Nano* 10 (2016) 4895–4919.
- [14] Y. Ma, X.L. Wang, Y.S. Jia, X.B. Chen, H.X. Han, C. Li, *Chem. Rev.* 114 (2019) 9987–10043.
- [15] H. Zhang, J.F. Banfield, *Chem. Rev.* 114 (2014) 9613–9644.
- [16] Y.B. Guo, Z.H. Zhang, Z. Ren, H.Y. Gao, P.X. Gao, *Catal. Today* 184 (2012) 178–183.
- [17] P.Q. Li, H.T. Hu, J.F. Xu, H. Jing, H. Peng, J. Lu, C.X. Wu, S.Y. Ai, *Appl. Catal. B-Environ.* 147 (2014) 912–919.
- [18] C.H. Kim, B.H. Kim, K.S. Yang, *Carbon* 50 (2012) 2472–2481.
- [19] J. Zhang, Q. Xu, Z.C. Feng, M.J. Li, C. Li, *Angew. Chem. Int. Ed.* 47 (2008) 1766–1769.
- [20] J.H. Park, S. Kim, A.J. Bard, *Nano Lett.* 6 (2006) 24–28.
- [21] Z.H. Zhao, J. Tian, Y.H. Sang, A. Cabot, H. Liu, *Adv. Mater.* 27 (2015) 2557–2582.
- [22] J. Sun, Y. Yang, J.I. Khan, E. Alarousu, Z. Guo, X. Zhang, Q. Zhang, O.F. Mohammed, *ACS Appl. Mater. Interfaces* 6 (2014) 10022–10027.
- [23] C. Di Valentin, G. Pacchioni, *Catal. Today* 206 (2013) 12–18.
- [24] Y.F. Shen, T.Y. Xiong, T.F. Li, K. Yang, *Appl. Catal. B-Environ.* 83 (2008) 177–185.
- [25] H.Y. He, J.H. Lin, W. Fu, X.L. Wang, H. Wang, Q.S. Zeng, Q. Gu, Y.M. Li, C. Yan, B.K. Tay, C. Xue, X. Hu, S.T. Pantelides, W. Zhou, Z. Liu, *Adv. Energy Mater.* 6 (2016) 1600464.
- [26] W.J. Zhou, Z.Y. Yin, Y.P. Du, X. Huang, Z.Y. Zeng, Z.X. Fan, H. Liu, J.Y. Wang, *H. Zhang, Small* 9 (2013) 140–147.
- [27] J. Tian, Z.H. Zhao, A. Kumar, R.I. Boughton, H. Liu, *Chem. Soc. Rev.* 43 (2019) 6920–6937.
- [28] J. Zhang, Z.P. Zhu, Y.P. Tang, K. Mullen, X.L. Feng, *Adv. Mater.* 26 (2014) 734–738.
- [29] J. Tian, Y.H. Sang, Z.H. Zhao, W.J. Zhou, D.Z. Wang, X.L. Kang, H. Liu, J.Y. Wang, S.W. Chen, H.Q. Cai, H. Huang, *Small* 9 (2013) 3864–3872.
- [30] K.X. Wang, C.L. Shao, X.H. Li, X. Zhang, N. Lu, F.J. Miao, Y.C. Liu, *Catal. Commun.* 67 (2015) 6–10.
- [31] D. Barreca, G. Carraro, A. Gasparotto, C. Maccato, M.E.A. Warwick, K. Kaunisto, C. Sada, S. Turner, Y. Gonullu, T.P. Ruoko, L. Borgese, E. Bontempi, G. Van Tendeloo, H. Lemmetyinen, S. Mathur, *Adv. Mater. Interfaces* 2 (2015) 1500313.
- [32] H.L. Wang, L.S. Zhang, Z.G. Chen, J.Q. Hu, S.J. Li, Z.H. Wang, J.S. Liu, X.C. Wang, *Chem. Soc. Rev.* 43 (2014) 5234–5244.
- [33] S. Anandan, T.N. Rao, M. Sathish, D. Rangappa, I. Honma, M. Miyauchi, *ACS Appl. Mater. Interfaces* 5 (2013) 207–212.
- [34] A. Du, Y.H. Ng, N.J. Bell, Z. Zhu, R. Amal, S.C. Smith, *J. Phys. Chem. Lett.* 2 (2011) 894–899.
- [35] Y.H. Zhang, Z.R. Tang, X.Z. Fu, Y.J. Xu, *ACS Nano* 4 (2010) 7303–7314.
- [36] S. Sakthivel, H. Kisch, *Angew. Chem. Int. Ed.* 42 (2003) 4908–4911.
- [37] J. Liu, H. Bai, Y. Wang, Z. Liu, X. Zhang, D.D. Sun, *Adv. Funct. Mater.* 20 (2010) 4175–4181.
- [38] Y.R. Yang, P. Gao, Y. Wang, L.N. Sha, X.C. Ren, J.J. Zhang, Y.J. Chen, T.T. Wu, P.P. Yang, X.B. Li, *Nano Energy* 33 (2017) 29–36.
- [39] F.Z. Jia, Z.P. Yao, Z.H. Jiang, C.X. Li, *Catal. Commun.* 12 (2011) 497–501.
- [40] B.C. Qiu, M.Y. Xing, J.L. Zhang, *J. Am. Chem. Soc.* 136 (2014) 5852–5855.
- [41] T. Hu, J.X. Yang, X.H. Wang, *Phys. Chem. Chem. Phys.* 19 (2017) 31773–31780.
- [42] X.H. Sang, Y. Xie, M.W. Lin, M. Alhabeab, K.L. Van Aken, Y. Gogotsi, P.R.C. Kent, K. Xiao, R.R. Unocic, *ACS Nano* 10 (2016) 9193–9200.
- [43] J. Etzko, M. Ade, H. Hillebrecht, *Inorg. Chem.* 46 (2007) 7646–7653.
- [44] H. Zhang, T. Hu, X.H. Wang, Z.X. Li, M.M. Hu, E. Wu, Y.C. Zhou, *Sci. Rep.* 5 (2015) 14192.
- [45] H. Zhang, T. Hu, Z.X. Li, Y.H. Zhang, M.M. Hu, X.H. Wang, Y.C. Zhou, *J. Am. Chem. Soc.* 100 (2017) 724–731.
- [46] Y. Wen, T.E. Rufford, X. Chen, N. Li, M. Lyu, L. Dai, L. Wang, *Nano Energy* 38 (2017) 368–376.
- [47] Y. Tang, J.F. Zhu, W.L. Wu, C.H. Yang, W.J. Lv, F. Wang, *J. Electrochem. Soc.* A923–A929 (2017).
- [48] Y. Yoon, M. Lee, S.K. Kim, G. Bae, W. Song, S. Myung, J. Lim, S.S. Lee, T. Zyung, K.S. An, *Adv. Energy Mater.* 8 (2018) 1703173.
- [49] A. Djire, H. Zhang, J. Liu, E.M. Miller, N.R. Neale, *ACS Appl. Mater. Interfaces* 11 (2019) 11812–11823.
- [50] N.T. Son, P.N. Hai, E. Jánzén, *Phys. Rev. B* 63 (2001) 201201.
- [51] N.T. Son, X.T. Trinh, L.S. Lovlie, B.G. Svensson, K. Kawahara, J. Suda, T. Kimoto, T. Umeda, J. Isoya, T. Makino, T. Ohshima, E. Janzen, *Phys. Rev. Lett.* 109 (2012) 187603.
- [52] P. Urbankowski, B. Anasori, T. Makaryan, D. Er, S. Kota, P.L. Walsh, M. Zhao, V.B. Shenoy, M.W. Barsoum, Y. Gogotsi, *Nanoscale* 8 (2016) 11385–11391.
- [53] X.L. Hu, S.C. Lu, J. Tian, N. Wei, X.J. Song, X.Z. Wang, H.Z. Cui, *Appl. Catal. B-Environ.* 241 (2019) 329–337.
- [54] C.Y. Mao, F. Zuo, Y. Hou, X.H. Bu, P.Y. Feng, *Angew. Chem. Int. Ed.* 53 (2019) 10485–10489.